

ASCA Observations of the Supernova Remnant VRO42.05.01

Zhiyu Guo and David N. Burrows

Department of Astronomy & Astrophysics, Pennsylvania State University,
525 Davey Lab, University Park, PA 16802;

I: guo@astro.psu.edu

I: burrows@astro.psu.edu

ABSTRACT

We present the results of our *ASCA* SIS and GIS observations of the supernova remnant VRO42.05.01. Our spectral fits indicate that the SNR is isothermal ($\sim 8.3 \times 10^6$ K), consistent with our *ROSAT* analysis results. The absorbing column density ($\sim 2.9 \times 10^{21}$ cm $^{-2}$) obtained from these spectral fits is much smaller than expected for the nominal distance of 5 kpc, indicating that the line of sight toward VRO42.05.01 has an unusually low gas density. The spectral resolution of *ASCA* allows us to determine elemental abundances for the hot X-ray emitting plasma in the bright “wing” component of this remnant. We find that Mg, Si, and Fe are underabundant, and attribute these low abundances to the galactic metallicity gradient and to the location of the remnant in the outer Milky Way.

Subject headings: ISM: supernova remnants — ISM: individual (VRO42.05.01)

1. Introduction

VRO42.05.01 (G166.0+4.3) is classified as a composite supernova remnant (SNR), with a shell-like radio morphology and a centrally-peaked X-ray morphology. Radio continuum observations (Landecker et al. 1982; Pineault, Landecker, & Routledge 1987) reveal an unusual shape, with a northeastern circular component (the “shell”) intersected by a much larger bowl-shaped component in the southwest (the “wing” component), which bears a remarkable resemblance to numerical models by Tenorio-Tagle, Bodenheimer, & Yorke (1985) of blast waves expanding across a density discontinuity. The morphology suggests that this SNR has broken out of the cloud within which it formed, expanded across an interstellar tunnel or cavity, and is now interacting with the material that forms the opposite tunnel wall (Pineault et al. 1987).

Optical observations find line ratios in the optical filaments of VRO42.05.01 characteristic of supernova remnants (Fesen, Blair, & Kirshner 1985; Pineault et al. 1985) and a filamentary structure similar to that observed in the radio continuum (Fesen, Gull, & Ketelsen 1983; Pineault et al. 1985). Shock velocities of over 100 km s^{-1} are implied by the optical data (Fesen et al. 1983; Lozinskaya 1979).

Burrows & Guo (1994, hereafter Paper I) presented the first X-ray images and spectra of VRO42.05.01, based on *ROSAT* PSPC observations. We found that the overall shape of the X-ray remnant is similar to that of the radio remnant, but that the X-ray image differs from the radio morphology in that the former is centrally-peaked instead of edge-brightened. The X-ray morphology is consistent with the evaporating cloud model of White & Long (1991). We also found that the X-ray data are consistent with an isothermal remnant ($\sim 8.5 \times 10^6 \text{ K}$) with variations in absorbing column density ($\sim \text{a few} \times 10^{21} \text{ cm}^{-2}$) across the remnant. We noted that the absorbing column obtained from the X-ray data is surprisingly small for the nominal distance of 5 kpc, which requires a low mean density along this line of sight.

In this paper, we present the results from our analysis of data obtained from two Solid-state Imaging Spectrometer (SIS) detectors and two Gas Imaging Spectrometer (GIS) detectors on board the Japanese X-ray satellite *ASCA* (Tanaka, Inoue, & Holt 1994). We shall describe the data acquisition and analysis in §2, discuss the physical implication of the data analysis results and a comparison with former results in §3, and present our conclusions in §4.

2. Data and Analysis

VRO42.05.01 was observed by the *ASCA* between 9 March 1994 and 11 March 1994 with two SIS detectors (4 CCD mode) and two GIS detectors (PH mode) in use simultaneously. Three pointings covered virtually the entire remnant with exposure times of 20 ks to 30 ks in each pointing. Standard event screening has been applied to both SIS and GIS observations using XSELECT (V1.2). The screening procedures include removal of hot and flickering pixels from the SIS observations, selection of usable field and background rejection based on rise time interval for the GIS observations, and selection of good observation time intervals. Hot and flickering pixel counts are found to comprise more than 95% of the total counts from each CCD chip, and more than 99% in some CCD chips. Cleaned SIS and GIS images of the SNR are shown in Figures 1 and 2 (Plates 00 and 00).

Even in the CCD chip that covers the brightest portion of the SNR, there are less

than 3500 counts left after cleaning the data. This has made our original goal of studying the spectral properties across the SNR on angular scales smaller than the detector size impractical. Instead, we have combined all of the events from each CCD to produce spectra of $11' \times 11'$ sized regions of the remnant. Only three pairs of the SIS CCD chips that cover the brightest portions of the SNR were able to provide spectra with sufficient signal to noise to allow spectral fits with reasonable statistics. These three CCD chip pairs are SIS0 CCD2 / SIS1 CCD0 in the first pointing (marked as Region 1 in Figure 1), SIS0 CCD0 / SIS1 CCD2 in the third pointing (Region 2), and SIS0 CCD3 / SIS1 CCD1 in the second pointing (Region 3). The GIS spectra were extracted from these same three regions. The energy ranges of both SIS and GIS spectra are from 0.6 keV to ~ 2.2 keV (gold edge). Blank sky event lists created by the *ASCA* GOF were used for background subtraction in all the spectral fits due to the limited number of background counts in our observations. Spectra from the GIS3 were binned to 128 PI channels (instead of 256) because of the telemetry problem for the GIS3 data in this particular observation period. No distinct emission lines are seen in any of the spectra. We show the SIS0 spectrum from Region 1, which covers the brightest portion of the SNR, in Figure 3.

Spectral fits to a variety of thermal models were performed using XSPEC (V9.01) for both the SIS and the GIS data sets. We were unable to obtain acceptable results in simultaneous fits to data from the same region of the SNR from all four detectors, suggesting an inconsistency between the SIS and the GIS. We therefore only used the two SIS spectra from each pointing and obtained reasonable results after adjusting the detector gain by a few percent. We tried to fit our spectral data using single temperature and two temperature Raymond-Smith models with solar abundances but were not able to obtain acceptable fits ($\chi^2/\text{d.o.f.}$ are 299/112 and 282/110, respectively). The centrally-peaked X-ray morphology and lack of emission lines are suggestive of a nonthermal source, but we could not obtain an acceptable fit to a power law spectrum ($\chi^2/\text{d.o.f.}$ is 314/112). We then tried using a non-equilibrium ionization (NEI) model with solar abundances produced by Richard Edgar at CfA, but still could not obtain a satisfactory fit ($\chi^2/\text{d.o.f.}$ is 251/111). The SIS spectra and images were compared with a 2-D hydrodynamical model produced by Jon Slavin at GSFC, which modeled a blast wave crossing a density discontinuity and integrated the plasma emissivity along various lines of sight to produce spectral simulations. With appropriate model parameters (explosion energy and location, and ISM density contrast) this model could approximate either the spatial appearance of VRO42.05.01 or its approximate spectral shape, but we were unable to satisfy both spatial and spectral observations simultaneously.

We were finally able to obtain acceptable spectral fits using a Raymond-Smith model with variable abundances. The fit results of the SIS spectra from the three brightest

portions of the SNR are given in Table 1 and are shown in Figures 3– 5 . The best fit model spectrum for Region 1 is plotted as a heavy histogram overlaid on the data in Figure 3. Low abundances of Mg, Fe, and Si are required to reproduce the nearly featureless observed spectrum. By comparison, the light histogram in Figure 3 shows the best fit Raymond-Smith model with solar abundances, which is too faint below 0.8 keV and has discrepancies at 1.26 keV and 1.85 keV associated with lines from Mg and Si which are prominent in the model but are not observed in the data. Confidence contour plots of the abundances (Figure 5) show that all three elements must be below solar abundance in the wing component for the Raymond-Smith model to successfully fit the data.

3. Discussion

The *ASCA* spectral fit results presented in Table 1 and Figure 4 confirm our previous *ROSAT* results that the SNR is isothermal and that the absorbing column densities towards Region 1 and Region 2 are consistent with each other but quite different from that towards Region 3. The temperatures obtained here are in reasonable agreement with those determined on the basis of our *ROSAT* observation. The emission measures obtained here cannot be directly compared with those from Paper I, because the regions included in the fit are not identical. The column density results are puzzling. Both data sets indicate a substantial difference in the absorbing column between the shell and wing components, but the sense is reversed: the *ROSAT* data indicate a smaller N_{H} for the wing component, while the *ASCA* data indicate a smaller N_{H} for the shell component. We are inclined to trust the *ROSAT* data in this case because the fitted column density is sensitive to the calibration of the lowest *ASCA* channels, which may not be entirely secure. However, it is possible that the absorbing gas is patchy and that the discrepancy found here is real. In any case, these column densities imply a low mean density for this line of sight, for the reasons discussed in Paper I. Further observations may be required to resolve this discrepancy.

Unlike N_{H} confidence contours (Figure 4), contours of elemental abundances (Figure 5) do not show clear differences between the wing and shell components. The confidence contours indicate that Mg and Si are underabundant in the wing component (Regions 1 and 2), while the abundances of these elements in the shell component are more uncertain and could be consistent with either solar abundances or with the depleted abundances found in the wing. The Fe abundances appear to be below solar values in both the wing and shell components. As shown in Figure 3, the low abundances are a consequence of the nearly featureless spectrum of this remnant. This is unusual, as most thermal SNRs have strong lines in their X-ray spectra.

VRO42.05.01 is an old SNR (2.4×10^4 yr, Paper I) and its X-ray emission should be dominated by emission from the swept-up ISM. The low abundances we find are therefore suggestive of low abundances in the local interstellar environment of the SNR. Since VRO42.05.01 is estimated to be 5 kpc from the Sun at galactic longitude 166° , the radial gradient of elemental abundances in the Milk Way may be responsible for the low abundances of this remnant. For a galactic radial metallicity gradient of -0.05 dex kpc^{-1} (Pagel 1981) in the neighborhood of the Sun, we estimate that the metallicity at the location of the remnant is 56% of solar. This is within the confidence contour ranges for Fe and Mg, and within a factor of 2 of the allowed range for Si. Taking into account the complication that galactic arms have higher elemental gradients (as large as -0.2 dex kpc^{-1} [Talent & Dufour 1979]), we would expect even lower abundances that are closer to our best fit values.

4. Conclusions

We conclude that the analysis of the *ASCA* data has shown consistent results with those from our *ROSAT* analysis. The SNR VRO42.05.01 is found to be isothermal with variations of neutral hydrogen column density across the remnant. The low column density suggests that the line of sight toward the SNR has an unusually low gas density. The important new result from the *ASCA* data is the first measurement of abundances in the hot plasma. The elemental abundances of Mg, Si, and Fe are found to be less than the solar abundance in the wing component where we have good statistics, but have a large uncertainty in the shell component where we have fewer counts. We attribute the low abundances to the galactic metallicity gradient and the resultant low metallicity in the swept-up ISM. This may explain the spectral differences between this remnant and 3C400.2, which has many similarities to VRO42.05.01 but has strong emission lines of Mg, Si, and Fe in its *ASCA* spectrum (Guo et al. 1997).

We would like to thank Eric Gotthelf at *ASCA* GOF for useful discussions on making the images, and Richard Edgar and Jon Slavin for providing NEI spectral models for comparison with our data. This work has been sponsored by NASA grant NAG5-2537.

REFERENCES

- Burrows, D. N., & Guo, Z. 1994, *ApJ*, 421, L19 (Paper I)
- Fesen, R. A., Blair, W. P., & Kirshner, R. P. 1985, *ApJ*, 292, 29
- Fesen, R. A., Gull, T. R., & Ketelsen, D. A. 1983, *ApJS*, 51, 337
- Guo, Z., Burrows, D. N., Dubner, G., Winkler, F., & Tsunemi, H. 1997, *ApJ*, in preparation
- Landecker, T. L., Pineault, S., Routledge, D., & Vaneldik, J. F. 1982, *ApJS*, 51, 115
- Lozinskaya, T. A. 1979, *Australian J. Phys.*, 32, 113
- Pagel, B. E. J. 1981, *ARA&A*, 19, 77
- Pineault, S., Landecker, T. L., & Routledge, D. 1987, *ApJ*, 315, 580
- Pineault, S., Pritchett, C. J., Landecker, T. L., Routledge, D., & Vaneldik, J. F. 1985, *A&A*, 151, 52
- Talent, D. L., & Dufour, R. J. 1979, *ApJ*, 233, 888
- Tanaka, Y., Inoue, H., & Holt, S. S. 1994, *PASJ*, 46, L37
- Tenorio-Tagle, G., Bodenheimer, P., & Yorke, H. W. 1985, *A&A*, 145, 70
- White, R. L., & Long, K. S. 1991, *ApJ*, 373, 543

Fig. 1.— The ASCA SIS image of VRO42.05.01 overlaid with 1420 MHz radio continuum contours (courtesy T. Landecker). The X-ray mosaic, which was smoothed with a $3'$ (FWHM) Gaussian, includes three pointings and combines counts from both SIS0 and SIS1. The three regions from which we extracted spectra are marked as boxes and are labeled Regions 1, 2, and 3.

Fig. 2.— Mosaic of *ASCA* GIS images from three pointings, smoothed with a $4.25'$ (FWHM) Gaussian. Overlaid contours are from the *ROSAT* $\frac{3}{4}$ keV image (Paper I).

Fig. 3.— SIS spectrum extracted from CCD chip 2 on SIS0 (Region 1). The data points are overlaid with the best Raymond-Smith model fit using a single temperature plasma with variable abundances (thick line) (Table 1), and the best Raymond-Smith model fit using a single temperature plasma with solar abundances (thin line).

Fig. 4.— Confidence contours for the fit parameters temperature (T) and absorbing column (nH). Dashed, solid, and dotted contours represent Regions 1, 2, and 3, respectively. Numbers ‘1’, ‘2’, and ‘3’ mark the best-fit values in each contour for the corresponding regions. The inner contours represent a confidence level of 70% ($\chi_{min}^2 + 7.23$) while the outer contours represent a confidence level of 90% ($\chi_{min}^2 + 10.64$).

Fig. 5.— Same as Figure 4, but for elemental abundances of Mg (upper), Si (middle), and Fe (lower) (relative to the solar abundance).

Table 1. X-ray spectral fit results from the *ASCA* SIS and the *ROSAT* PSPC data

Parameters CCD Pairs used	<i>ASCA</i> SIS			<i>ROSAT</i> PSPC ^b	
	Region 1 ^a	Region 2 ^a	Region 3 ^a	Wing	Shell
	S0C2 / S1C0 Wing	S0C0 / S1C2 Wing	S0C3 / S1C1 Shell		
Temperature (10^6 K)	7.8	8.3	8.3	8.1	8.6
N_{H} (10^{21} cm ⁻²)	2.9	2.8	0.7	1.3	2.6
Normalization (10^{11} cm ⁻⁵)	4.6	3.1	1.6	4.7	3.0
Mg abundance	0.27	0.33	1.02	N/A	N/A
Si abundance	0.026	0.0	0.40	N/A	N/A
Fe abundance	0.37	0.47	0.36	N/A	N/A
χ^2 /d.o.f.	194/109	167/96	158/97	12.6/15	3.75/15

^aThe three spectral regions are marked in Figure 1.

^bThe parameters for the ROSAT data are from Burrows and Guo (1994).

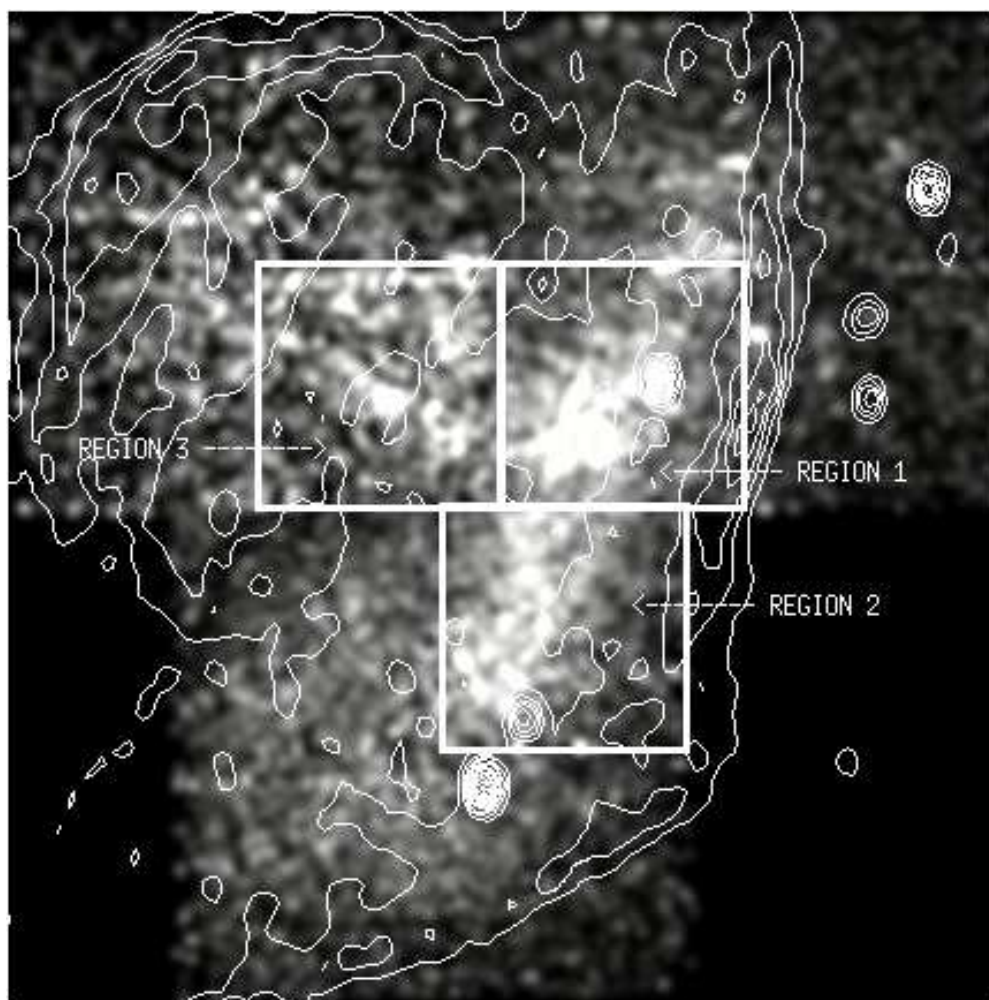


Fig. 1

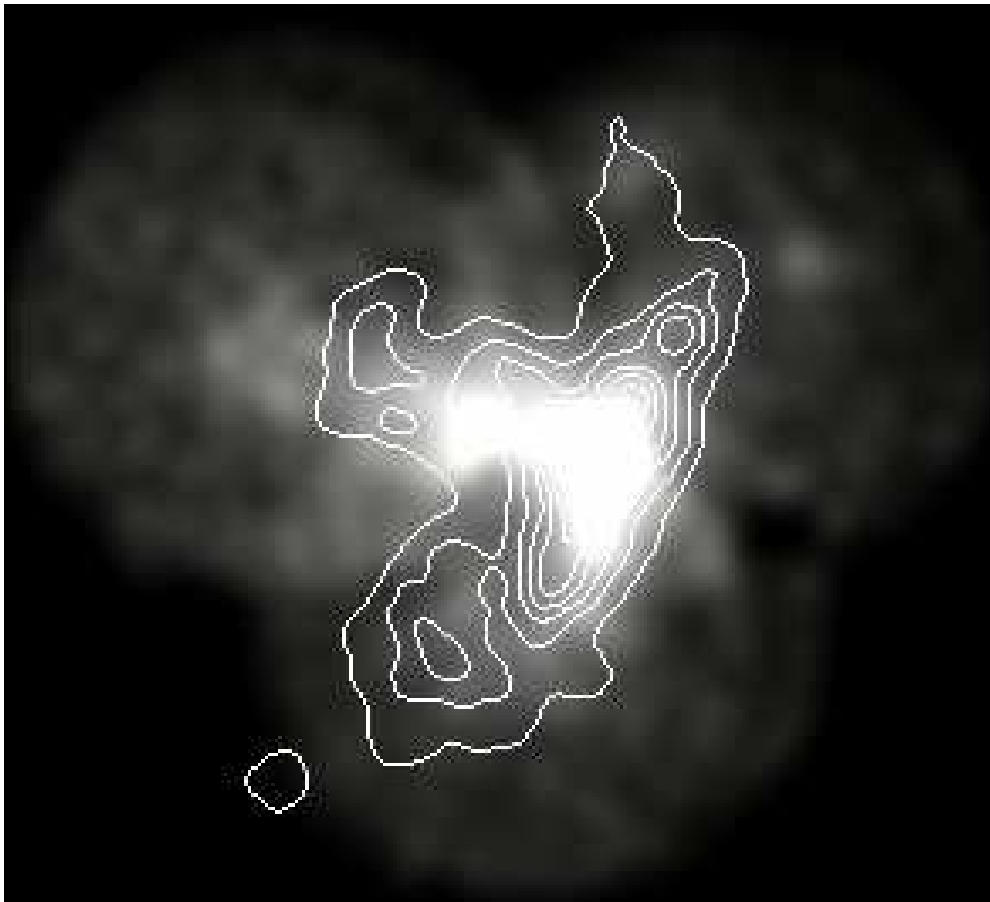


Fig. 2

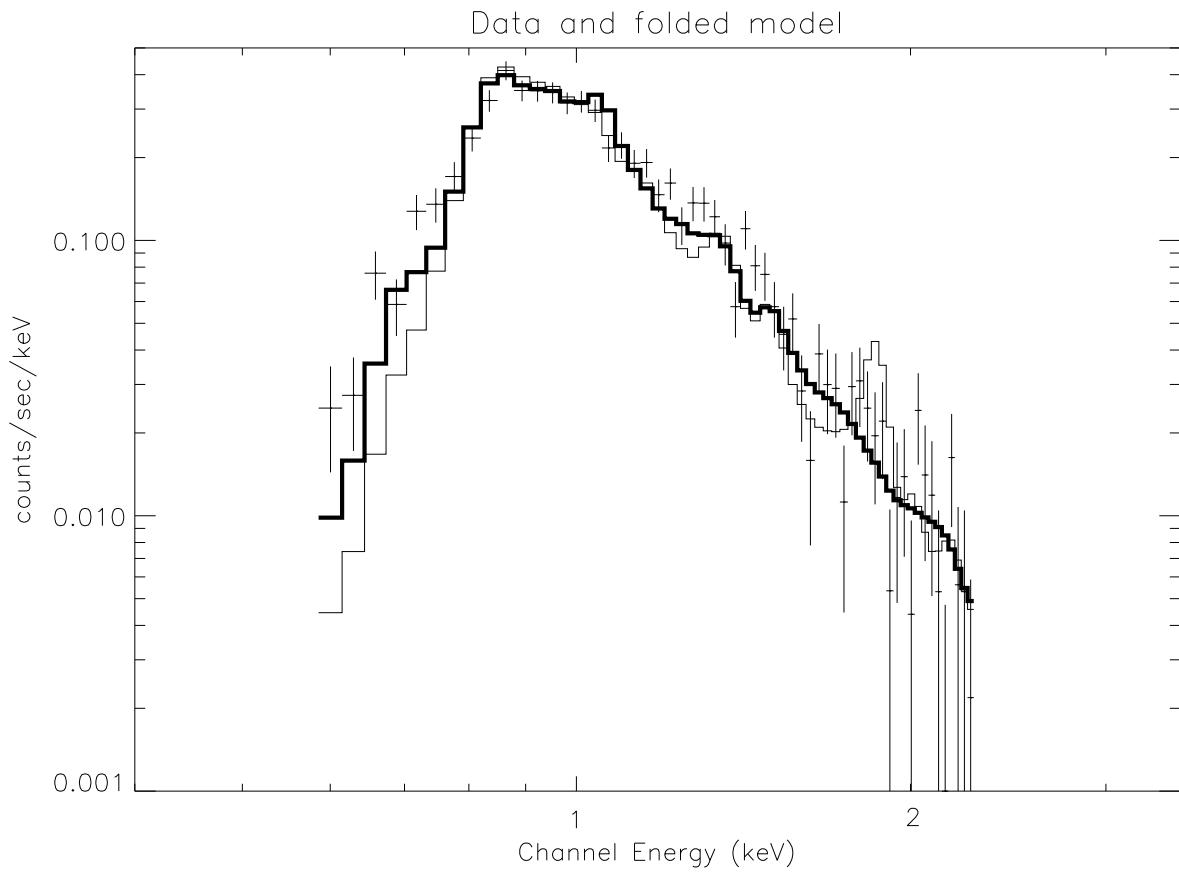


Fig. 3

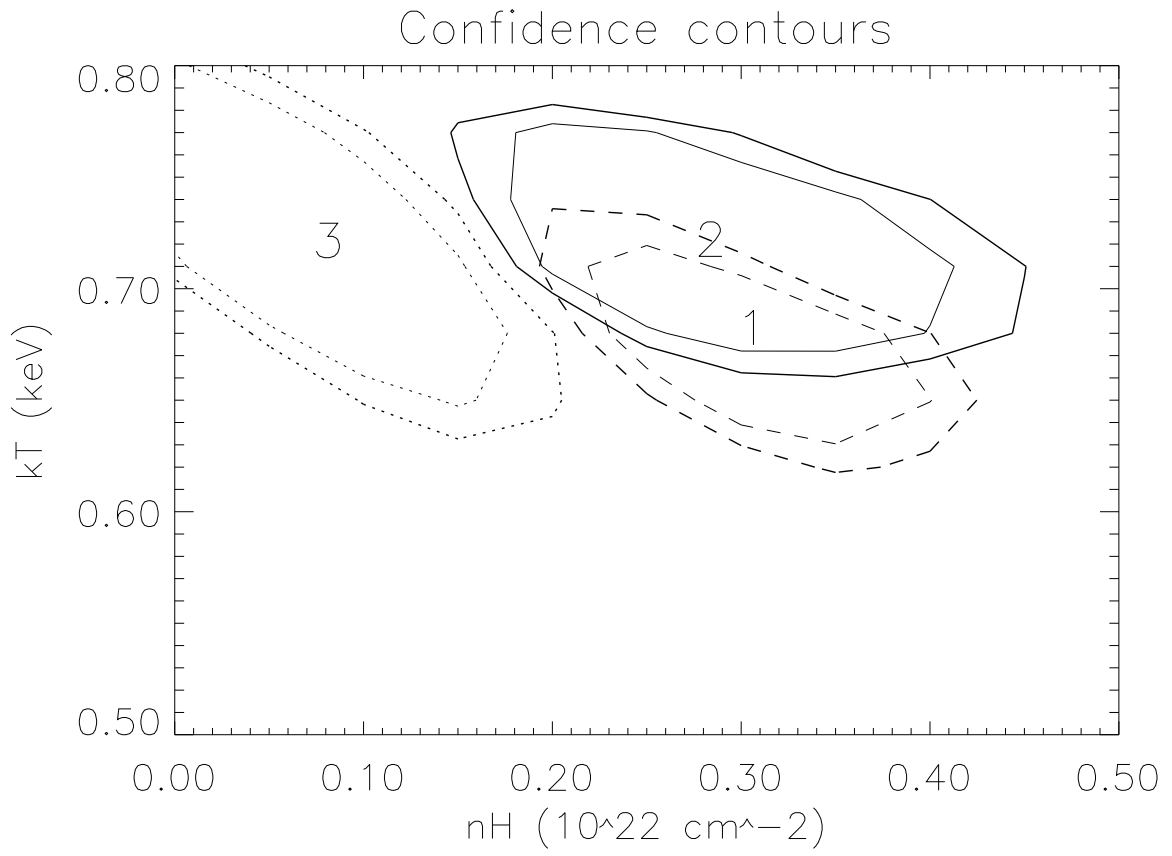


Fig. 4

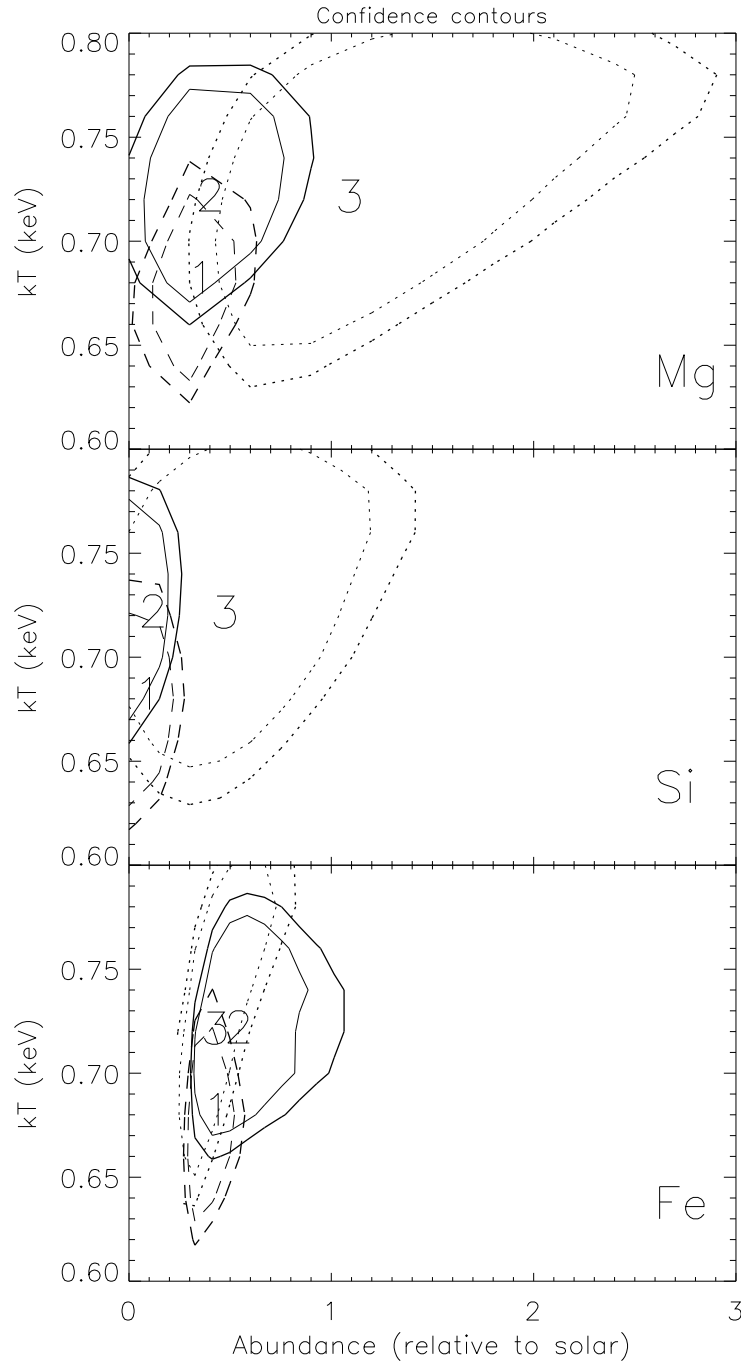


Fig. 5